Biofluid eye modeling for Spaceflight Associated Neuro-ocular Syndrome (SANS)

A thesis presented for the Bachelor's degree in
Aerospace Engineering

Dipartimento di Ingegneria Meccanica e Aerospaziale
Politecnico di Torino

Supervisor:
Stefania Scarsoglio

Candidate:
Luca Pascarito

Contents

Chapter 1

Introduction

1.1 Spaceflight associated neuro-ocular syndrome

Astronauts participating in space missions can be subject to physiological and structural changes due to the conditions of the environment they are exposed to, especially microgravity. One of the most important syndromes astronauts can develop is spaceflight associated neuro-ocular syndrome (SANS). It comprises different changes in ocular structure that can impair vision, and they can surface separately or together.

According to NASA's evidence report [1], the percentage of studied crewmembers who reported the onset of any of the SANS associated ocular findings ranges from 37.5% to 51%. Structural changes have been observed to persist to a certain degree even months after return on Earth, suggesting that they are permanent. Thus, SANS represents an important roadblock for human space exploration.

SANS comprises of one or more of the following ocular findings: hyperopic shift, cotton-wool spots, choroidal folds, optic disc edema, optic nerve sheath distention, and posterior globe flattening with varying degrees of severity and permanence.

Subjects affected by a hyperopic shift have better visual acuity at far distances rather than near, as a result of light entering the eye with a focal point which is posterior the retina due to the eye's refractive power.

Cotton-wool spots and choroidal folds, as well as optic disc edema, can be assessed by fundoscopy, a medical test in which, through an ophthalmoscope, the fundus of the eye (the interior surface opposite the lens) can be seen and analyzed. In a funduscopy, the lighter circular area is the optic disc, while the darker one is the fovea, a very important part of the retina which, when light is focused on it, produces clear images. A cotton-wool spot is characterized as an opaque white patch on the retina, while choroidal folds are alternating lines, grooves or striae that appear as alternating light and dark lines, as can be seen in Figure 1.1. Optic disc edema consists in the swelling of the optic disc with a concurrent increase in fluid within or surrounding the axons (see Figure 1.2).

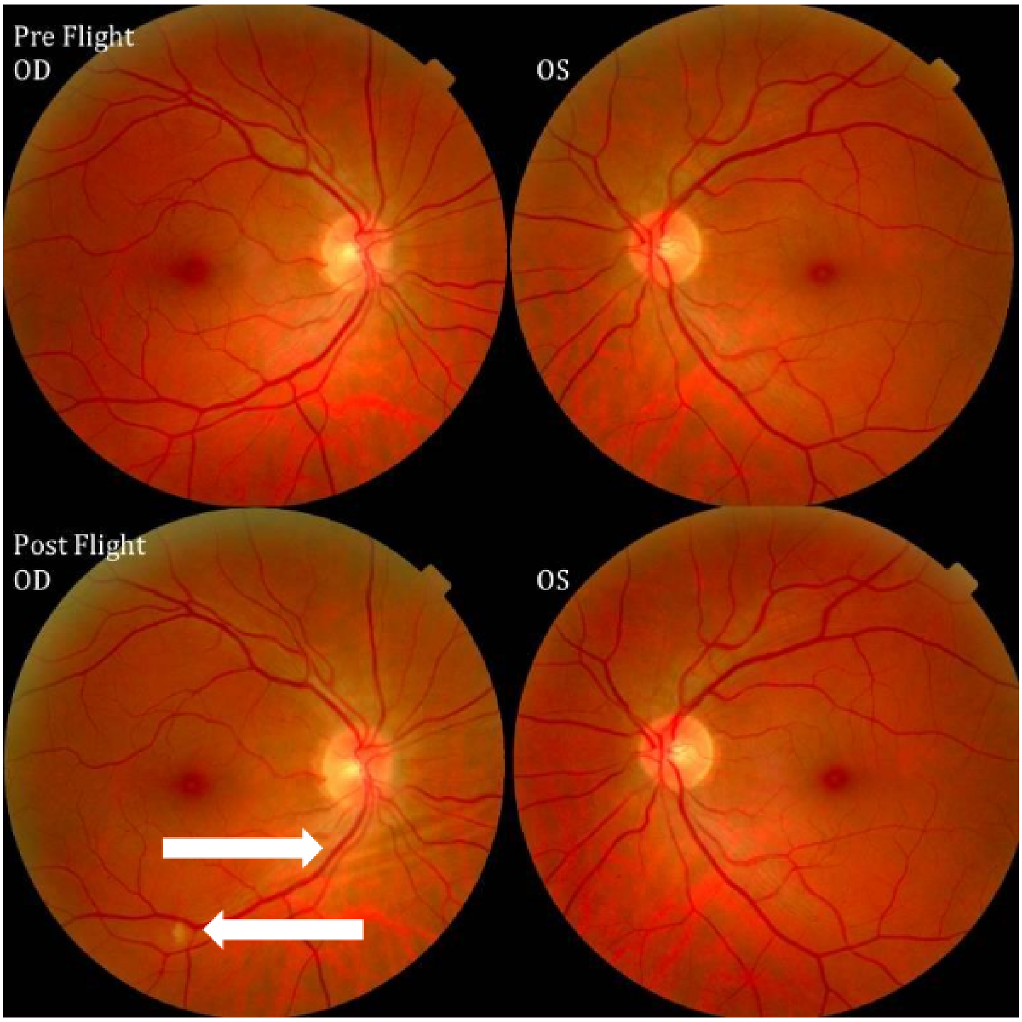

Figure 1.1: *Fundus examination of a case of vision change from long-duration spaceflight, in which a single cotton-wool spot and choroidal folds can be seen in the inferior arcade of the right eye. "OD" refers to the right eye image, while "OS" refers to the left one. Both pre-flight and post-flight images are shown. Taken from [1]*

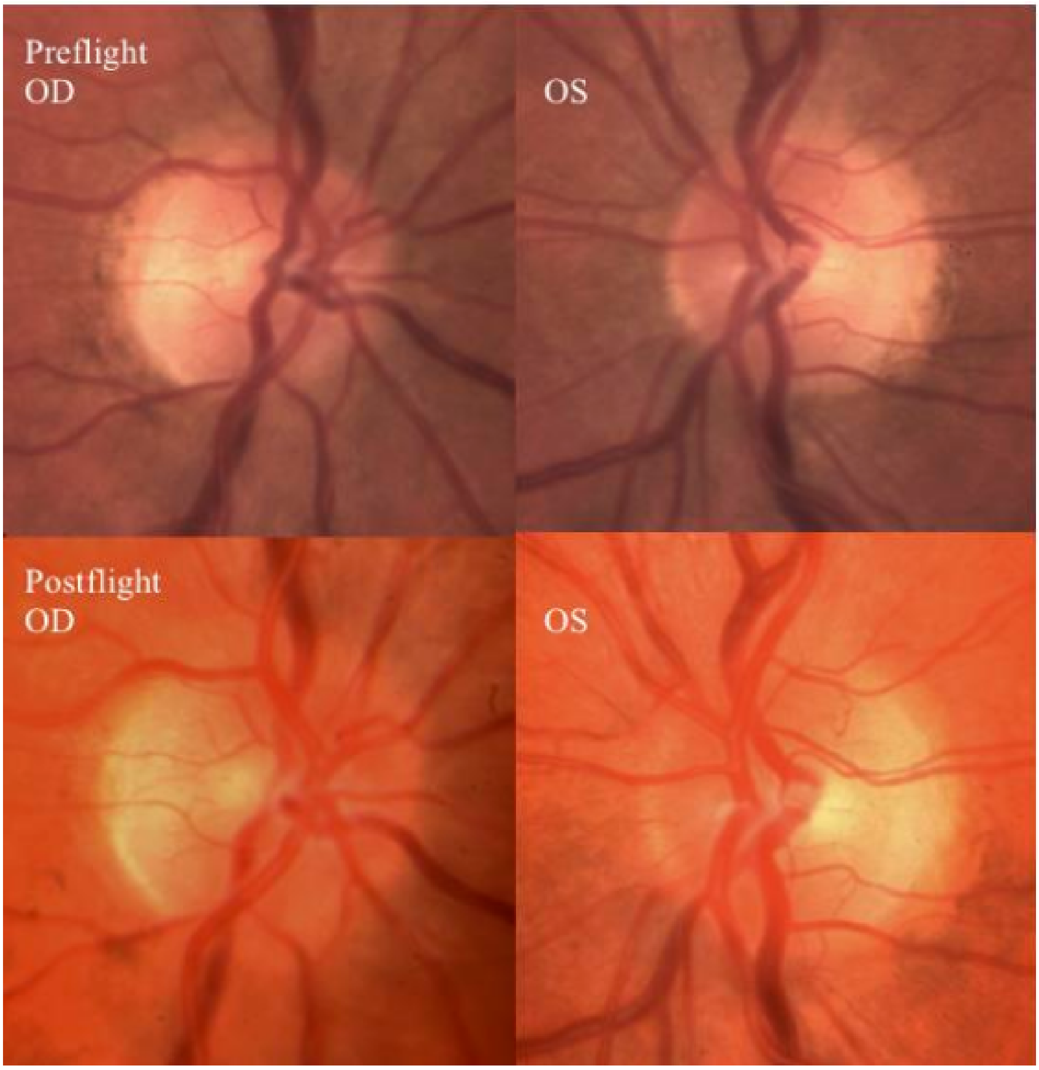

Figure 1.2: *Fundus examination of an astronaut who reported vision changes resulting from long-duration spaceflight: preflight images show normal optic discs, while postflight images show the right optic disc suffering from grade 1 disc edema (nasal and superior). Taken from [1]*

Globe flattening is a result of structural change in the globe, as can be seen in Figure 1.3, where it is concurrent with elevation of the optic disc (consistent with disc edema), while increased optic nerve sheath diameter (ONSD) can be seen in Figure 1.4. Both figures are ultrasound images obtained on-orbit from the same astronaut.

SANS symptoms and associated ocular findings are similar to those expe-

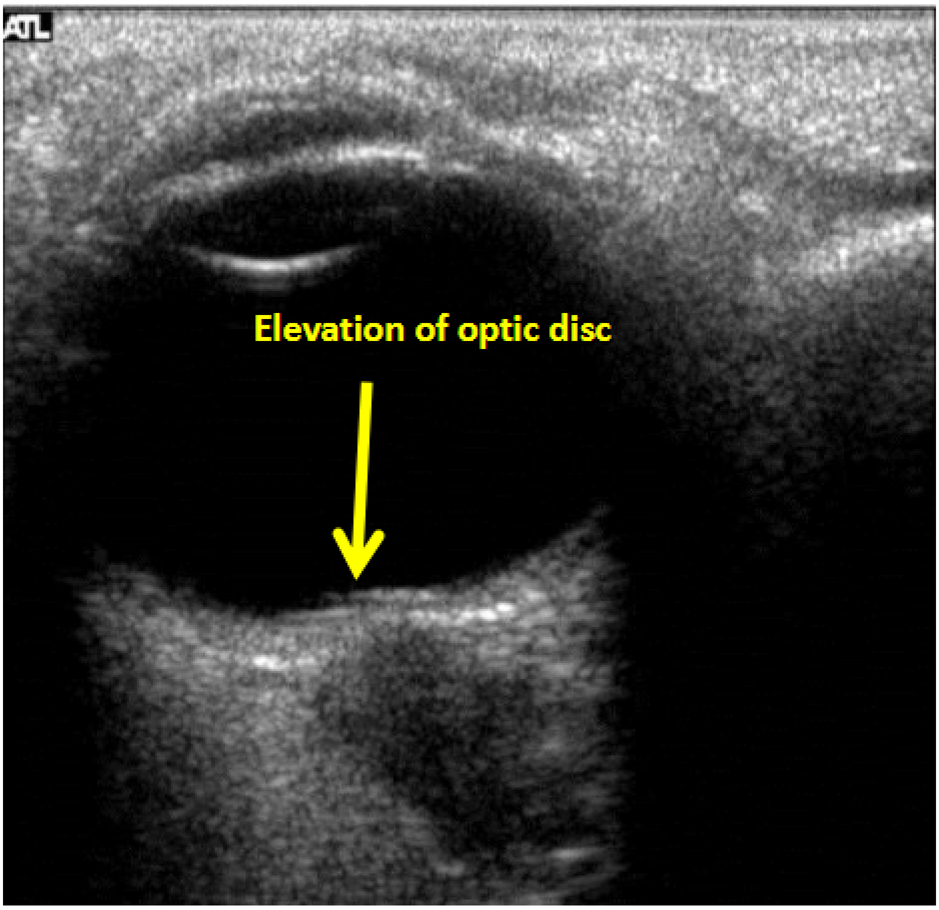

Figure 1.3: *On-orbit ultrasound image showing posterior globe flattening and a raised optic disc consistent with optic disc edema. Taken from [1]*

rienced on Earth in idiopathic intracranial hypertension (IIH), a condition caused by raised intracranial pressure (ICP), which is why at first SANS was named visual impairment and intracranial pressure (VIIP). Astronauts who suffer from SANS, though, have not reported experiencing often other symptoms of IIH such as frequent headaches [1]. The variation of ICP in long-flight missions is still not clearly understood. This is due to the fact that the gold standard for measuring ICP is lumbar punctures, which are an invasive measurement method, and ICP measurements during long-flight missions are still lacking.

Variations of intraocular pressure (IOP) are thought to play a role in the onset of SANS, as it is noted to increase in microgravity and possibly cause stress on the eye structures. Elevated IOP is also a high risk factor for glaucoma, so understanding its behavior is crucial to study visual impairment

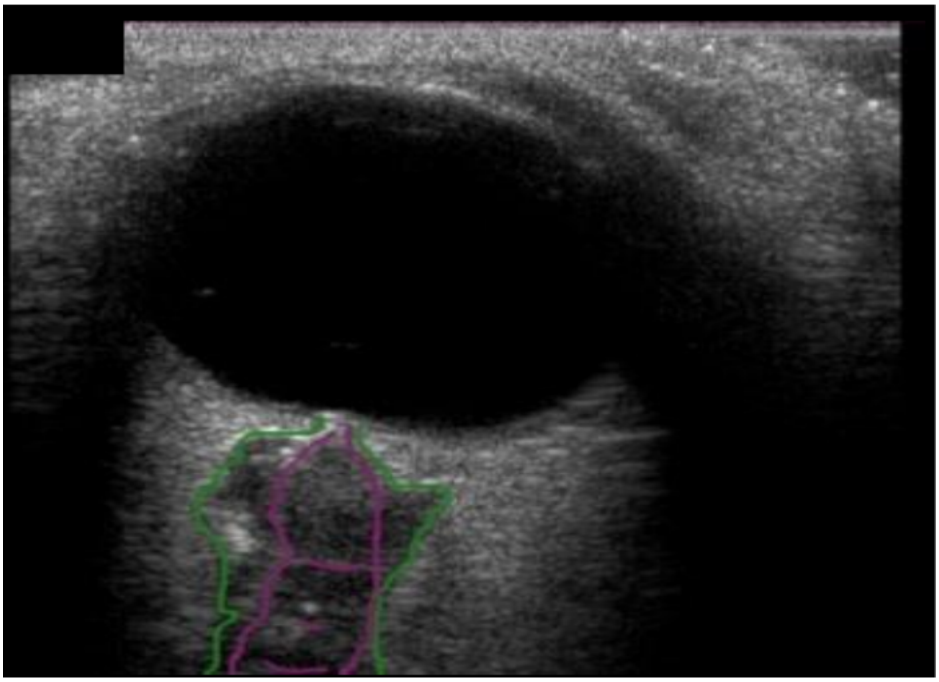

Figure 1.4: *On-orbit ultrasound image showing increased ONSD (shown in green, optic nerve shown in purple) of approximately 12 mm. Taken from [1]*

and propose countermeasures.

The etiology and pathophysiology of SANS is still being investigated. Since the difficulty in obtaining on-orbit measurements and reliable results between studies, mathematical models can be a great tool to investigate the effects of microgravity conditions on the eyes. In this thesis, after briefly introducing the anatomy of the eye, models for eye hemodynamics will be discussed both for on Earth (experiencing 1g of gravitational acceleration) and in microgravity simulations.

In chapter 2, the essential anatomy of the eye is introduced, explaining its structure, composition, and its arterial vessels through the study of the ophthalmic artery. Chapter 3 and 4 present different mathematical models simulating ocular hemodynamics respectively in 1g and in microgravity conditions. Lumped-parameter models, called 0D (zero-dimensional), are introduced and explained, both for simplicity and because other types of hemodynamic simulations of the eye in microgravity do not exist yet in literature. These models are then coupled with a 1D (one-dimensional) model of the cardiovascular system, to have a better understanding of the autoregulation mechanisms at play in microgravity. In chapter 5, conclusions from the findings and results of the different simulations are drawn.

Chapter 2

Anatomy of the eye

2.1 Structure of the eye

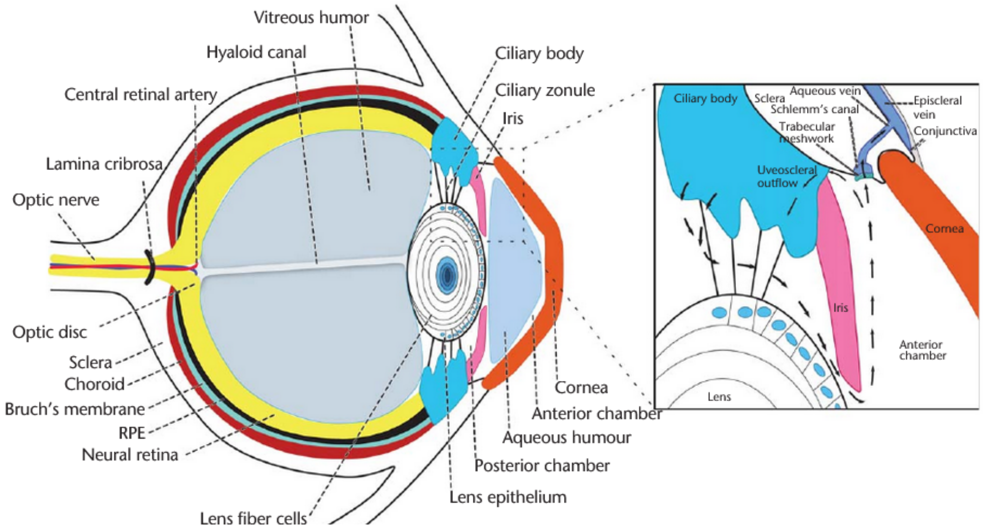

Figure 2.1: *Schematic of a vertebrate eye taken from [2]*

The anatomy of the eye has been summarized by Zhu et al. [2], a schematic of which can be seen in Figure 2.1. Approximately two-thirds of the eye volume is occupied by vitreous humor, composed by 99% of water with a small amount of collagen. It occupies the cavity between the lens and the retina.

The retina is extremely important for vision, as it is made up of neural cells that process light signals into neural ones. Studying the effects of microgravity conditions on retinal structure and hemodynamics is a necessary step to understand SANS.

The lamina cribrosa (LC) is a porous, collagenous cylindrical structure [1] on which ICP and IOP act upon, thus being a key component in structural consequences of pressure equilibrium.

The optic nerve serves as the pathway connecting the retina to the brain's visual processing center. The optic disc, or optic nerve head (ONH) is the area where the optic nerve crosses through the posterior fundus of the eye, and has a diameter of approximately 1.5 mm.

The ciliary body is a circumferential tissue surrounding the lens, composed of ciliary muscle (which can change the degree of refraction of the lens), ciliary zonule (thin, peripheral ligaments that suspend and hold the lens in place) and ciliary epithelium (it secretes aqueous humor).

The aqueous humour is produced by the ciliary body in the posterior chamber, from where it flows into and fills the anterior chamber. It is constantly replenished: most of it flows through the trabecular meshwork into Schlemm's canal and episcleral veins, while the rest follows the uveoscleral route, by percolation through the interstitial tissue spaces of the ciliary muscle, continuing to pass into the suprachoroid and leaving through the sclera. Its balance is a critical factor for determining IOP.

2.2 Anatomy of the Ophthalmic Artery

The anatomy of the ophthalmic artery (OA) was reported by Michalinos et al. [3] through a bibliographic search. The OA is the first intracranial branch of the internal carotid artery (ICA) and arises after the ICA emerges from the cavernous sinus, from where it follows a short intracranial course to enter the the orbit through the optic canal. There it ramifies and vascularizes the eyeball and the periophtalmic tissues, branching also in the central retinal artery (CRA), that is of critical importance for vision.

The OA has a measured diameter between 0.7 and 1.8 mm. According to a study by Hayreh and Dass [4], it arises above the dura and follows an intradural course in 83.6% of cases, while in 6.6% of cases it arises just above dura and in 10% of cases it arises below dura and follows a total or partial extradural course, with other researchers publishing similar results. Percentages for localization of the arising OA in ICA walls are not universally consistent through studies.

This study assumes that variant OA patterns are due to migration, partial or complete regression and persistence of primitive vessels during embryonic life. The most common variant is the OA origin from the middle meningeal artery (MMA), but also dorsal OA (a primitive vessel that supplies the eyeball in the early embryonic state together with ventral OA and MMA). In these cases, the OA enters the orbit through superior optic fissure rather than the optic canal, and clinical effects can be noted. OA origin from MMA can lead to blindness in case of accidental or surgical traumatism or in case of MMA embolization due to head and neck tumors or persistent epistaxis. In some rare cases, the MMA arises from the OA due to anastomosis between MMA and internal maxiliary artery (IMA) never developing or regressing. Variant origin from the anterior cerebral artery has also been reported, as well as double OA due to the persistence of ventral and dorsal primitive OA. Rare origin from middle cerebral artery and posterior communicating artery have been reported, and an extreme variation, namely OA originating from basilar artery, has been reported twice, but finds no conclusive explanation.

After originating, OA follows an intracranial path of 0.5 to 9.5 mm according to [4], creating one or two angles (it does not follow a straight path). In this area, branches of the OA are the deep recurrent OA, which is a remnant from embryologic dorsal OA that anastomoses with a branch of the inferolateral trunk, and superficial recurrent OA, which anastomoses with the marginal tentorial artery.

The OA then passes below the posterior edge of the falciform ligament, piercing the dura matter of the optic nerve (ON) usually inferiorly and laterally, and alongside with the ON enters the optic canal, which is of small length, usually from 5 to 7 mm. According to literature, in approximately 6.7% of cases the origin of the OA from the ICA is found anterior to the falciform ligament, and in very rare cases (<3%) it passes to the orbit separate from the ON, through another separate bony canal.

The course of the OA in the orbit is divided in 3 parts: first, it courses inferiorly and laterally to the ON after exiting the optic canal; then, it courses medially passing above (in 83% of cases) or below (17%) to the ON; finally, it is separated in its branches medially to the ON. Branching is complex and virtually unique between persons and eyes of the same person.

Branching is different in the case of OA passing above or below the ON. In the first case, usually: the first branch is a common trunk for a middle posterior ciliary artery (MPCA) and the CRA; the second branch is the lateral posterior ciliary artery (LPCA); the third branch is the lacrimal artery (LA); the fourth branch is a common trunk, for superior rectus and levator muscles; the fifth branch is for posterior ethmoidal and supraorbital arteries; the sixth branch is another MPCA; seventh and eighth branches are muscular; ninth branch is anterior ethmoidal; tenth branch is inferior or medial inferior palpebral; and eleventh branch is superior palpebral; then, it divides to dorsal nasal and supraorbital artery.

If the OA passes below the ON: first branch is LPCA; second is CRA;

third is medial muscular; fourth is MPCA; fifth is LA; sixth is a muscular branch to superior rectus and levators; seventh is a common trunk for posterior ethmoidal and supraorbital; eighth is a common trunk for superior oblique and medial rectus; ninth is anterior ethmoidal; tenth is inferior medial palpebral; eleventh is superior medial palpebral; then, it divides to frontal artery and dorsal nasal artery.

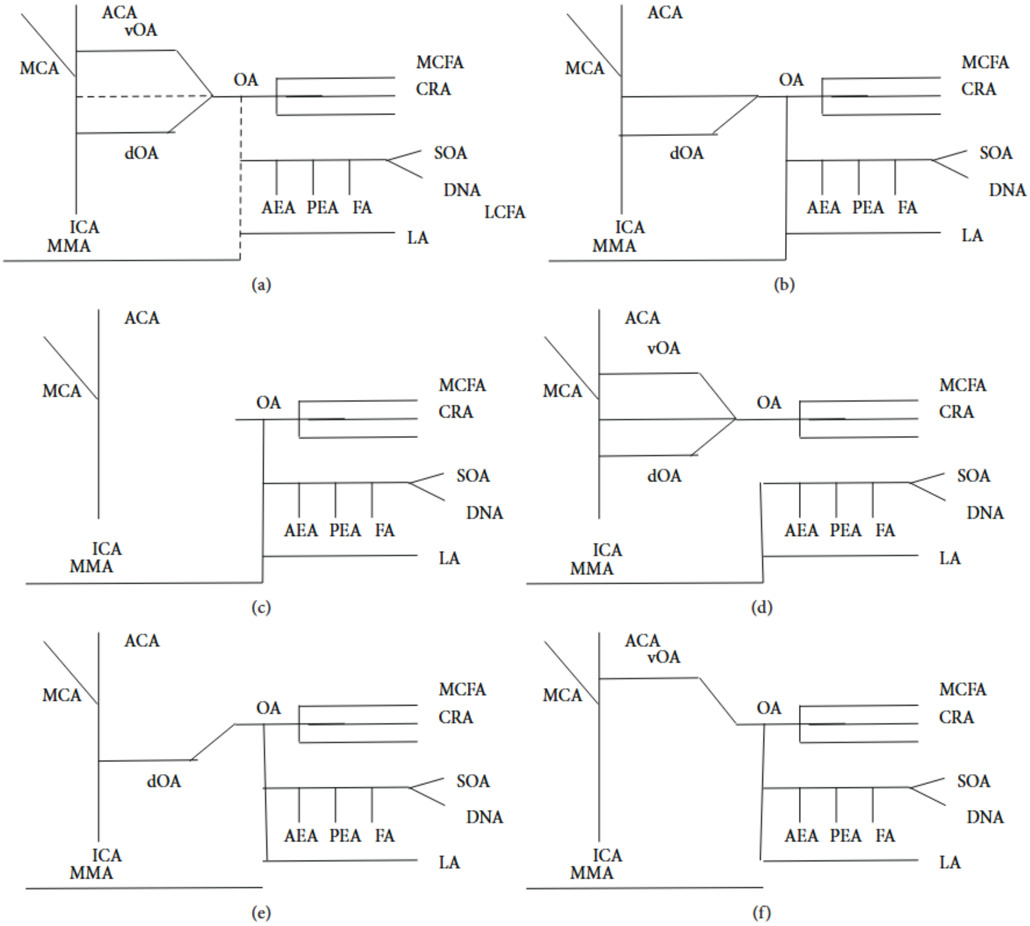

Figure 2.2: *Highly schematic representation of most common OA variations. (a) represents most common anastomosis patterns with dotted lines; (b) is the typical anatomical pattern. From (c) to (f) variations are, in order: OA originating from MMA; persistent dorsal and ventral OA (dOA and vOA); LA originating from MMA; persistent dOA; persistent vOA (OA originating from anterior cerebral artery, ACA. MCA: middle cerebral artery; AEA and PEA: anterior and posterior ethmoidal arteries; FA: frontal artery; SOA: supraorbital artery; DNA: dorsal nasal artery. Taken from [3]*

The CRA is a terminal branch that supplies the inner layer of the retina, thus retaining a fundamental role for vision. It is usually (77.5% of cases) the first branch, and in most cases (58.7%) it originates between the first and second part of the intraorbital OA, otherwise it originates in the first or in the second part. It can arise independently (37.5% of cases), in a common trunk with MMA (49.1%), with LPCA(11.5%), or in a common trunk with both MMA and LPCA (1.9%). CRA length varies between 7 and 20 mm, with a diameter ranging from 0.1 and 0.6 mm. It follows a tortuous course before piercing the dura of the ON and entering the retina. In less than 2% of cases a duplicated CRA was found. After entering the retina, it divides into inferior and superior branch, which further divide into temporal and nasal branches. Cilioretinal arteries represent an anatomic variation: they usually supply the temporal half of the retina, and they are present in 6-32% of people, with 14-18% of cases of them being bilateral, according to literature investigated by [3].

Posterior ciliary arteries directly supply the choroid and outer layers of the retina, playing a critical role in visual function. Their number can vary from 1 to 5, though in 80% of cases they are 2 or 3. According to their position they are termed or lateral, while the existence of superior or inferior posterior ciliary arteries is inconsistent. After originating, they divide into multiple short arteries that supply the proximal choroid and ON head, then they pierce the sclera and continue as long ciliary arteries that supply the distal choroid, the iris and the choroid body. Behind the lamina cribrosa, posterior arteries anastomose in a circle shape in what is called the circle of Zinn. LPCA and MPCA both have a diameter of 0.5-0.7 mm.

The lacrimal artery (LA) supplies lacrimal branches and adjacent muscular and periorbital tissues: it branches in glandular artery (that supplies the lacrimal gland), lateral palpebral artery, a small recurrent meningeal branch and muscular branches. Its diameter is approximately 0.7 mm. Embryologically, it originates from MMA, but this prototype persists in adult life in 28% of the cases. Normally, a recurrent branch connects MMA and OA with anastomosis taking place at the apex of superior optical fissure.

Two ethmoidal arteries arise from the OA: a larger one, the anterior ethmoidal artery (diameter of approximately 0.6 mm) and the posterior ethmoidal artery (diameter of approximately 0.4 mm). The former supplies ethmoidal air cells and the periosteum, and it enters the cranial cavity through anterior ethmoidal foramen, becoming the anterior meningeal artery. The posterior ethmoidal artery supplies the superior oblique, the superior and medial recti, and the levator, as well as sometimes the nose and ethmoidal air sinuses. Less commonly, they supply the falx and dura in the anterior cranial fossa, the periosteum and aeolar tissue in the orbit, and very rarely the sphenoid air sinus.

The supraorbital, frontal and dorsal nasal arteries have in common exclusive supply to periorbital and extracranial tissues. Superior orbital is a small branch that courses at the upper side of the orbit, gives small muscular branches and branches to areolar tissues, terminating by supplying the scalp. Frontal artery and dorsal nasal arteries are terminal branches of the OA, as it exits the orbit, and respectively supply the scalp and the nose.

The OA has a rich anastomotic network that, in case of occlusion, acts protectively: in the case of acute proximal occlusion of the OA, vision remains in 90% of cases in individuals without systemic vascular disease. Specifically, a deep anastomotic network is formed between IMA and OA, and the most important anastomosis is the one formed between OA and MMA.

2.2.1 Investigation using superselective angiography

OA morphology was studied by Akdemir Aktaş et al. [5] evaluating angiographies performed on children (age 4-120 months) with intraocular retinoblastoma undergoing intra-arterial chemotherapy. Angiography permits to measure internal arterial diameter, while studies on cadavers measure external diameter after perfusion, fixation and dehydration which alter elasticity and diameter of vessels. Origin and branching of OA seems consistent with findings from [3], but Aktaş et al. find supraorbital artery arising before termination of the OA. Angiography images are reported in Figures 2.3,2.4,2.5

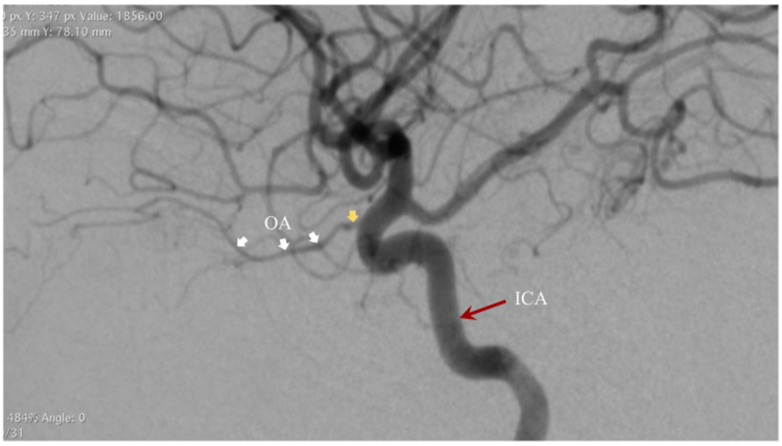

Figure 2.3: *ICA in the lateral projection, showing its course and the OA. Taken from [5]*

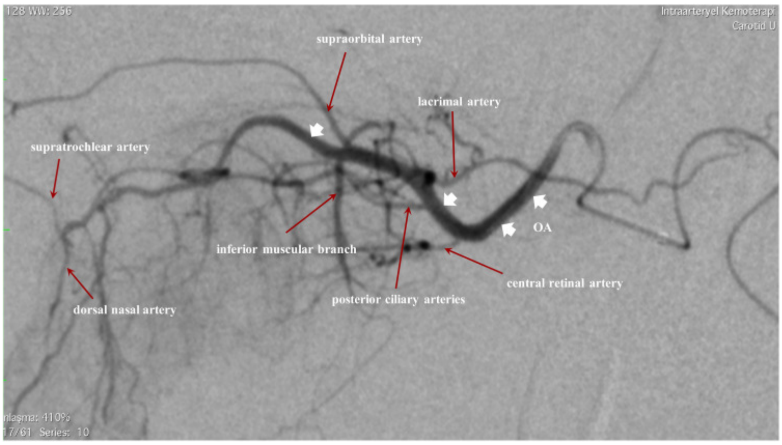

Figure 2.4: *Courses of the OA and its branches shown through superselective angiography. Taken from [5]*

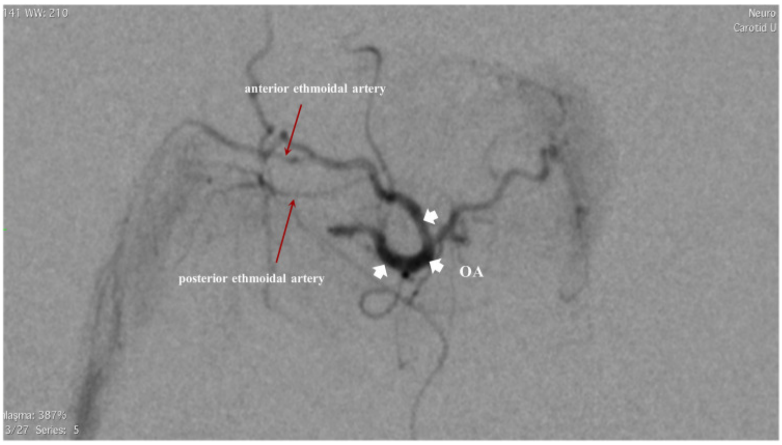

Figure 2.5: *Posterior and anterior ethmoidal arteries shown through superselective angiography of OA in the ipsilateral oblique projection. Taken from [5]*

The branches with higher angiographic visibility are the posterior ciliary arteries, LA, inferior muscular branch and AEA. CRA has a low visibility because it is a thin vessel that courses among several others. The results on measurements of the diameter of vessels are summarized in Table 2.1.

A total of 134 patients were included in the study, 57 of which were girls and 77 were boys.

The diameter of OA was found not to change with age, while the diameter of dorsal nasal artery was found to increase with age. Some arteries in girls were found to have a slightly smaller diameter than in boys (while posterior

Table 2.1: *Mean±SD (mm) of orbital arteries by sex. Taken from [5]*

Variables	**Total**	**Girls**	**Boys**
Ophthalmic artery	0.79±0.15	0.76±0.14	0.80±0.15
Central retinal artery	0.24±0.07	0.24±.06	0.25±0.07
Posterior ciliary arteries	0.26±0.07	0.27±0.07	0.24±0.07
Lacrimal artery	0.35±0.12	0.36±0.12	0.35±0.12
Inferior muscular branch	0.32±0.09	0.31±0.08	0.33±0.10
Supraorbital artery	0.22±0.07	0.21±0.08	0.23±0.06
Posterior ethmoidal artery	0.24±0.08	0.23±0.06	0.25±0.09
Anterior ethmoidal artery	0.29±0.08	0.28±0.07	0.30±0.08
Supratrochlear artery	0.25±0.09	0.22±0.07	0.27±0.11
Dorsal nasal artery	0.23±0.06	0.22±0.06	0.24±0.07

ciliary arteries follow an inverse trend). The authors of the study hypothesized that arteries may be more affected by levels of hormones such as estrogen than the others, but this was not confirmed by any large study, and the mechanisms underlying sex difference in arterial diameter also need more investigating.

2.2.2 Anatomic Features through Computed Tomography

Another contribution was made by Xu and Liu [6] using separating, fusing, opacifying and false-coloring, volume rendering (SFOF-VR) technique, which offers 3D imaging to highlight ICA and OA anatomic parameters (see Figure 2.6).

Using the technique on 109 healthy subjects divided in three age groups (young age, middle age, old age) they measured the diameters of the ICA's sixth segment (ICA-C6, according to Bouthiller classification the one from which OA originates) and OA, the length of ICA, the distance from the origin of the OA to the ON, and the angle between OAs and the median line.

The results indicated that male and female have statistically significant differences in right ICA-C6 and right OA diameters, bilateral distances between OA and ON, and lengths of bilateral ICA-C6.

Classifying patients with age, a statistical difference was observed in the bilateral lengths of ICA-C6 and in its left diameter, which became more evident with age. ICA-C6 length and diameter also increased with age.

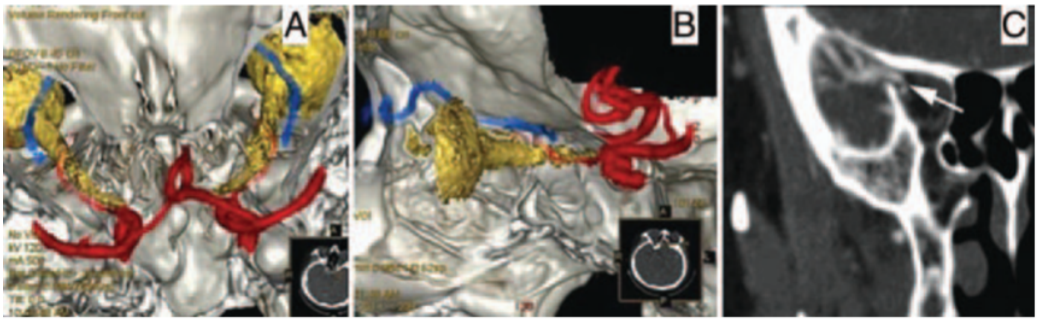

Figure 2.6: *(A) and (B): SFOF-VR imaging of cranial-orbital region, with nerves in yellow, ophthalmic arteries in red and superior ophthalmic veins in blue, bone structures in white. (C): maximum projection imagin of OA, with the arrow indicating the right OA origin from meninges. Taken from [6]*

2.3 Measuring Blood Flow in the Ophthalmic Artery

The eye blood flow is fundamental for visual functions. The arterial flow is mainly provided by the OA which is generally the first branch of the carotid artery and exits the cranial cavity through the optic canal. In addition to steady flow, during each heartbeat there is a pulsatile component due to cardiac pulsations that generates a cyclic distension of the OA and its branches, producing changes in intraocular volume and resulting in the cardiac pulsations seen in the intraocular pressure recordings.

Disturbed ocular blood flow is believed to be associated with the progression of ocular disorders such as macular degeneration, diabetic retinopathy and glaucoma, and impaired arterial blood supply to the eye can be a marker of vascular diseases such as retinal artery embolus, temporalis arteritis, and other forms of ischemic eye diseases.

In 2013, Phase-Contrast Magnetic Resonance Imaging (PCMRI) was used to measure OA hemodynamics to verify its precision and feasibility in contrast to Color Doppler Imaging (CDI), then regarded as the technique of choice for such measuring. However, with CDI accurate measurement of flow in the OA is difficult and invasive, as it can interfere with pressures inside the eye and, as such, can alter normal vascular conditions , whereas PCMRI is a non-invasive technique that does not interfere directly with the eye pressure. The study was conducted on 50 healthy young (HY) and 44 healthy elderly (HE) individuals. Measuring the cross-sectional area and the mean velocity within the left and right OAs with PCMRI, the mean blood flow was computed as their product. The volume of arterial pulsatility ΔV was also computed, and the Resistive

Index (RI) was calculated as

$$RI = \frac{Q_{syst} - Q_{diast}}{\Delta V} \tag{2.1}$$

where Q_{syst} and Q_{diast} are the systolic and diastolic peaks of the flow rate Q. Data from PCMRI were reconstructed to provide 32 phases (velocity-mapped) and magnitudes (anatomic) images throughout one entire cardiac cycle.

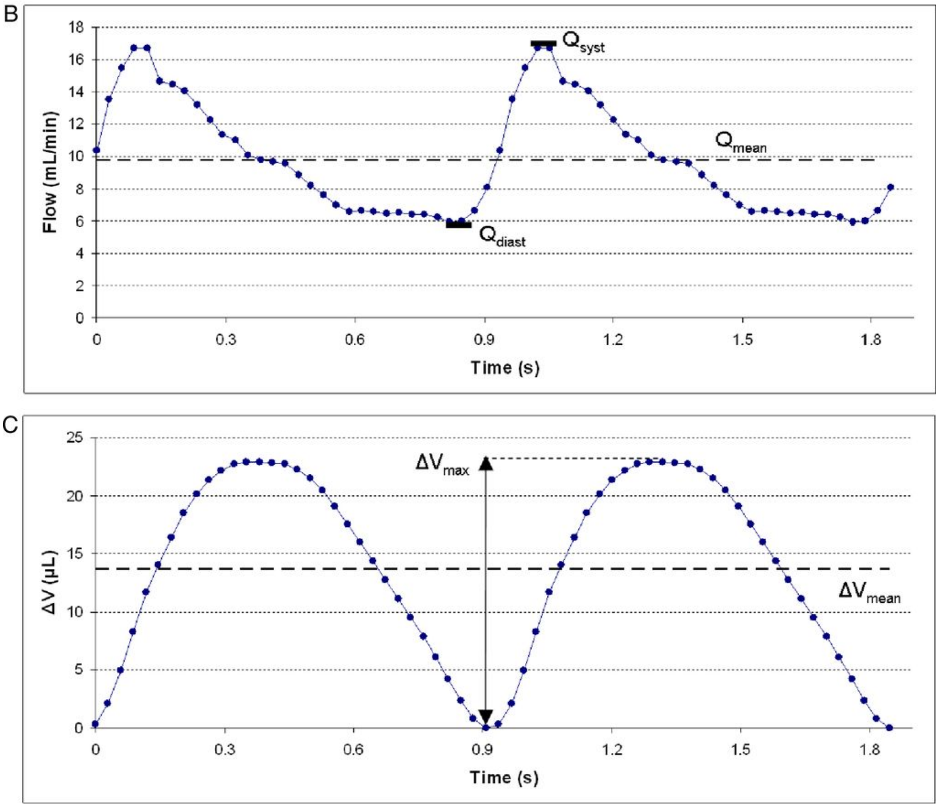

Figure 2.7: *B) represents the ophthalmic artery blood flow in a healthy young individual; C) represents the corresponding volume of arterial pulsatility. Taken from [7]*

No significant differences were observed between the flow parameters of the left and right OAs both in the HY and the HE groups. The systolic flow velocities were $U_{syst} = 16.97 \pm 4.63\, cm/s$ in HY and $U_{syst} = 16.88 \pm 5.57\, cm/s$ in HE, while the diastolic ones were $U_{diast} = 6.32 \pm 2.57\, cm/s$ in HY and $U_{diast} = 5.48 \pm 2.42\, cm/s$ in HE. There was no statistical difference in the mean flow Q_{mean} between the two groups, though a significant difference was measured between males and females (Q_{mean} in males: $12.09 \pm 5.71\, mL/min$;

Q_{mean} in females: $9.30 \pm 3.36\, mL/min$). A difference in the flow curves between HY and HE was observed only in the relaxation phase after the systolic peak. ΔV and RI were found to be higher in HE ($\Delta V = 26.27 \pm 12.59\, \mu L$, $RI = 0.67 \pm 0.1$) than in HY ($\Delta V = 18.70 \pm 7.24\, \mu L$, $RI = 0.62 \pm 0.08$)

A vessel-phantom of 1.4 mm in diameter (to mimic the cross-sectional area of the human OA) was cast in agar and used to evaluate PCMRI accuracy against reference values. In these experiments, the relative error between PCMRI and reference values for the flow rates ranged from 1.7% to 6.5%.

The study found that PCMRI is a feasible method to study OA hemodynamics. The fact that, while Q_{mean} does not change with age, the pulsatility components do (ΔV was 44% higher in HE than in HY during the cardiac cycle), and the fact that the difference is most notable in the relaxation phase of the cardiac cycle indicate that the biomechanical properties of the vessels change with age. The slower relaxation in HE suggests that vascular resistance was higher, or that the vascular compliance was increased due to reduced elasticity (or a combination of the two). This would mean that with aging, capillary walls get an increased exposure to pulsatile stress.

Chapter 3

On-Earth models to simulate ocular hemodynamics

3.1 Lumped-parameter models

Given the difficulty of obtaining on-orbit non-invasive measurements, mathematical models are useful tools for investigating ocular hemodynamics.

Calculations of IOP and ICP, for example, as blood flow, may help understand the response in the eye to microgravity conditions and what happens at the onset of SANS. First, models that simulate on-Earth conditions, those being the presence of a gravitational vector of 1g, will be presented. Here the simulation is considered in a standing position.

To model ocular hemodynamics, researchers use lumped-parameter models (zero-dimensional). The eye is divided into lumped compartments (a simple schematic example can be seen in Figure 4.1) that interact with each other.

These compartments can then be treated as electrical components, creating an analogue electric circuit (an example can be seen in the first model that will be presented, see Figure 3.1). This concept is called hydraulic-electric analogy [8]. Resistors are used to simulate the hydraulic resistance of blood vessels, while variable resistances can be used to account for other mechanisms such as autoregulation [9] or transmural pressure difference [10].

Flow in the circuit is regulated by the following equations: the analogue of conservation of mass in the form of Kirchhoff's laws;

Ohm's law:

$$Q = \frac{\Delta P}{R} \tag{3.1}$$

where Q is blood or aqueous humour flow and ΔP is the difference of pressure between two nodes and R is the resistance;

Poiseuille's law:

$$R = \frac{k_r \rho L}{A^2} \tag{3.2}$$

where A is the representative cross-sectional area of the compartment, L is the representative compartment length, ρ is blood density, μ is blood dynamic viscosity and $k_r = \frac{8\pi\mu}{\rho}$.

Filtration between compartments is regulated by the Starling-Landis equation:

$$Q_{ij} = K_{ij}\left[(P_i - P_j) - \sigma_{ij}(\pi_i - \pi_j)\right] \tag{3.3}$$

where Q_{ij} is the flux due to filtration from the compartment i to the compartment j, P_i and π_i are the hydraulic and osmotic pressures in the compartment i, K_{ij} and σ_{ij} are the filtration and reflection coefficients from the compartment i to the compartment j [10].

3.2 The relationship between Intraocular Pressure, Blood Pressure and Retinal Blood Flow Autoregulation.

As Guidoboni et al. [9] summarized in the introduction to their 2014 article, various attempts have been made to assess the correlation between variations in IOP and consequent reactions in ocular hemodynamics, but there has been conflicting clinical evidence: for example, a number of clinical studies showed a decrease in retinal and retrobulbar blood flow and velocity with an increase in IOP while others showed no significant change in retinal and retrobulbar hemodynamics when IOP was increased. Conflicting results are probably due to different factors including arterial blood pressure and blood flow autoregulation which are difficult to evaluate in a clinical setting.

This is why [9] proposes a mathematical model to account for blood flow in the central retinal vessels, blood flow in the retinal microvasculature, retinal blood flow autoregulation, biomechanical action of IOP on the retinal vasculature, and time-dependent arterial blood pressure. In the model, the retinal vasculature is studied with an hydraulic analogy to Ohm's law, in which blood flow is treated as current flowing through resistances and capacitances,

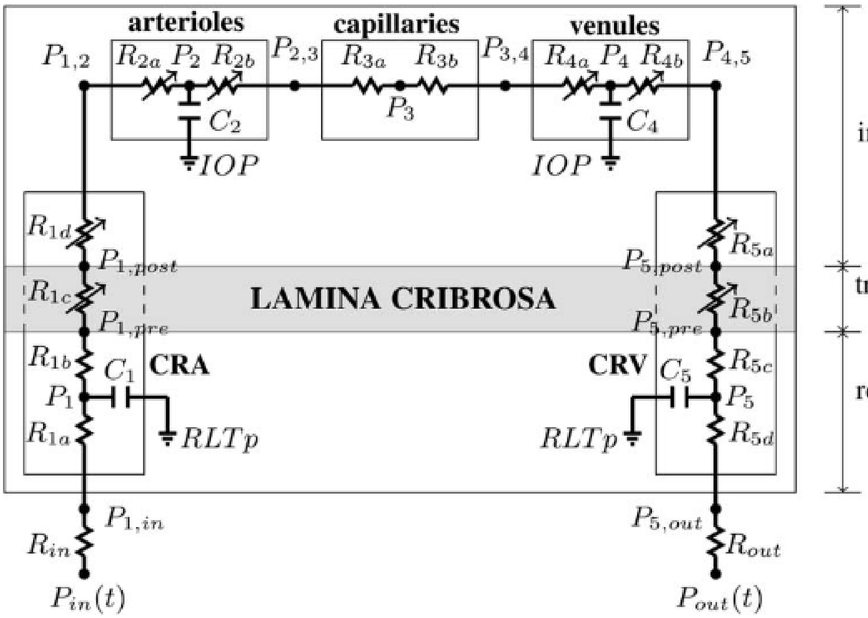

Figure 3.1: *Model for the retinal vasculature. It is divided in five main compartments: the central retinal artery (CRA), arterioles, capillaries, venules and the central retinal vein (CRV). The retrobulbar segments are exposed to retrolaminar tissue pressure (RLTp). Taken from [9]*

with variable resistances accounting for the variation of vessel diameter due to IOP and autoregulation of the blood flow.

The retinal vasculature is modeled as in Figure 3.1, divided in five compartments. Resistors represent the resistance to the flow, while capacitors represent the capacity of vessels to store blood volume and deform. The whole flow is regulated by P_{in} and P_{out}. The stress induced on the lamina cribrosa by IOP is calculated using a nonlinear elastic model. The resistances of venules and intraocular and translaminar CRA and CRV segments are assumed to vary passively, but arterioles' resistance is assumed to vary to achieve a relatively constant blood flow despite changes in ocular perfusion pressure (OPP).

Using Ohm's law ($Q = \Delta P/R$, where ΔP is the pressure difference between two nodes; also, for capacitors we consider $Q = c \times \mathrm{d}P/\mathrm{d}t$) and Kirchoff's law (at every node the volume change must be equal to the difference in inflow and outflow) we get the governing equations of the system:

$$c_1 \frac{d\,(P_1 - RLT_p)}{dt} = \frac{P_{in} - P_1}{R_{in} + R_{1a}} - \frac{P_1 - P_2}{R_{1b} + R_{1c} + R_{1d} + R_{2a}} \tag{3.4}$$

$$c_2 \frac{d\,(P_2 - IOP)}{dt} = \frac{P_1 - P_2}{R_{1b} + R_{1c} + R_{1d} + R_{2a}} - \frac{P_2 - P_4}{R_{2b} + R_{3a} + R_{3b} + R_{4a}} \tag{3.5}$$

$$c_4 \frac{d\,(P_4 - IOP)}{dt} = \frac{P_2 - P_4}{R_{2b} + R_{3a} + R_{3b} + R_{4a}} - \frac{P_4 - P_5}{R_{4b} + R_{5a} + R_{5b} + R_{5c}} \tag{3.6}$$

$$c_5 \frac{d\,(P_5 - RLT_p)}{dt} = \frac{P_4 - P_5}{R_{4b} + R_{5a} + R_{5b} + R_{5c}} - \frac{P_5 - P_{out}}{R_{5d} + R_{out}} \tag{3.7}$$

which are time-dependent because of variations in P_{in} and P_{out} during the cardiac cycle.

Control values are defined to set a normal state for a healthy individual, assuming blood and intraocular pressures and calculating the retinal blood flow Q using Poiseuille's law in the CRA. CRA and CRV resistances are also calculated with Poiseuille's law, while for arterioles, capillaries and venules resistances determining a control value is more complex. For the hierarchy of such vessels Guidoboni et al. considered the dichotomous network model elaborated by Takahashi et al. [11] which includes 14 levels of arterioles, 14 levels of venules and 1 level of capillaries, each with a number of parallel vessels. Parameters for the vessels (number, diameter, length...) were taken from [11] and corresponding lumped resistances were calculated. P_{in} is assumed to be 2/3 of the mean arterial pressure, while the control value for $P_{2,3}$ is taken from literature, and the pressure values in other nodes are obtained through Ohm's law, with P_{out} set lower than $P_{5,out}$ but higher than jugular venous pressure. The capacitances are computed as the product of vascular volume, which is computed, and distensibility, assumed to be equal to those of cerebral arteries for CRA and arterioles and, for venules and CRV, following Lakin et al. [12], eight times larger.

The model was used to study effects of altered arterial blood pressure and autoregulation on the hemodynamics of the retinal vasculature, as can be seen in Figure 3.2. For individuals with normal arterial blood pressure and functioning autoregulation, the average blood flow remained relatively constant over a cardiac cycle for values of IOP ranging from 15 to 23 mmHg, while for predictions based on subjects with high arterial blood pressure this was true for IOP values ranging from 23 to 29 mmHg. For predictions on individuals with low arterial blood pressure or without taking into account autoregulation, with IOP values ranging between 15 and 45 mmHg a slight or nonexistent autoregulation plateau was observed.

This model presents a virtual laboratory to study and isolate the contributions to retinal hemodynamics made by arterial blood pressure and autoregulation, from which predictions can be made on the susceptibility of tissues to IOP changes. The model predictions for velocity and flow in a control state are consistent with six independent studies, suggesting modeling choices are physiologically reasonable. With regards to the autoregulation plateau, the prediction that it shift towards higher IOP values as the mean arterial pressure increases is in agreement with a study He et al. [13] on Long-Evans rats. The flow velocity was predicted to not always decrease as an effect of increased IOP, specifically when autoregulation is achieved. In an individual with normal arterial blood pressure and functioning autoregulation, lowering IOP from 40 to 30 mmHg would produce a significant increase in total retinal blood flow and flow velocity in the CRA, while was IOP to be lowered from 25 to 15 mmHg, little hemodynamic changes would be observed. This would help explain the conflicting results in hemodynamic changes following trabeculectomy. Intraluminal blood pressure was also found to increase with IOP in all vascular compartments upstream of the CRV, consistently to experimental observations. Intraluminal arterial pressure would be affected differently depending on the functioning of the autoregulation mechanism.

Though useful in predicting retinal hemodynamic variations, a limitation of this model is the reduction of retinal vasculature in five compartments: including a more realistic geometry would help uncover changes in different retinal quadrants. Also, incorporating a mechanistic autoregulation mechanism, more realistic than the one proposed in this model, could help to get a larger autoregulation plateau consistent with clinical data and also investigate retinal hemodynamics in some cases of endothelial or metabolic dysfunction. Also, the lamina cribrosa is assumed circular, isotropic and homogenous, but its real geometric and mechanical characteristics are far more complex and vary with different factors such as age and ethnicity.

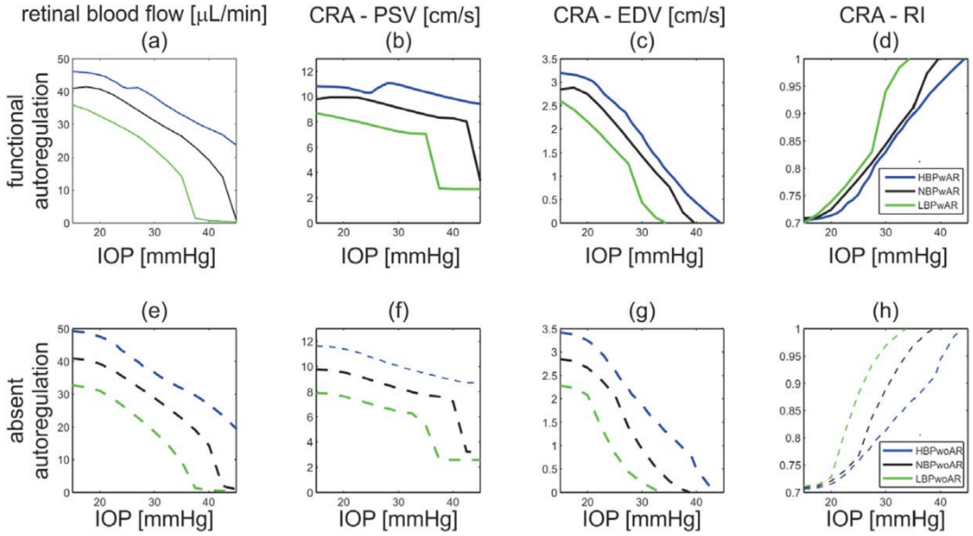

Figure 3.2: *Model predicted values of the different parameters for different theoretical patients. Taken from [9]*

3.3 Modeling of aqueous humor flow and intraocular pressure under uncertainty

The relationship between variations in aqueous humor (AH) flow parameters and IOP was studied by Szopos et al. [14], using a simplified mathematical model that describes the steady-state value of IOP as the result of the balance between AH production and drainage. The latter process is influenced by factors such as blood pressure in ciliary body capillaries (cBP), total inflow facility (L, flow rate per units of pressure), blood/AH oncotic pressure ($\Delta\pi_c$) and osmotic pressure difference ($\Delta\pi_s$), episcleral venous pressure (EVP), trabecular outflow facility (C_0), maximum uveoscleral flow rate (k_1).

AH production is the result of a passive mechanism called ultrafiltration, consisting in flow of transparent fluid across semipermeable membrane like vascular walls and epithelial cells, and an active mechanism called ionic secretion, proportional to blood/AH osmotic pressure difference. These flows are respectively modeled as follows:

$$Q_{ah,uf} = L[(cBP - IOP) - \sigma_p \Delta\pi_c] \tag{3.8}$$

$$Q_{ah,sec} = L(-\sigma_s \Delta\pi_s) \tag{3.9}$$

where σ_p is a protein reflection coefficient and σ_s is a reflection coefficient for low-molecular components. We can see $Q_{ah,uf}$ being proportional to the difference between cBP and IOP.

AH drainage is driven by passive mechanisms in two pathways, a "conventional" one called the trabecular pathway (AH passes through the trabecular meshwork into Schlemm's canal and then into episcleral veins), and a "non-conventional" one called the uveoscleral pathway (AH flows through ciliary muscle into supraciliary space). Flow through the trabecular pathway $Q_{ah,tm}$ is modeled as flow through a nonlinear resistor positioned between the anterior chamber (where pressure equals IOP) and episcleral veins (where pressure equals EVP), as proposed by Brubaker [15]. Flow through uveosclerar pathway $Q_{ah,uv}$ is modeled as flow through a nonlinear resistor connected to ground.

$$Q_{ah,tm} = C_{tm}(IOP - EVP) \tag{3.10}$$

$$with \quad C_{tm} = \frac{1}{R_0[1 + K_{ob}(IOP - EVP)]} \tag{3.11}$$

$$Q_{ah,uv} = C_{uv} \times IOP \tag{3.12}$$

$$with \;\; C_{uv} = \frac{k_1}{k_2 + IOP} \tag{3.13}$$

where C_{tm} and C_{uv} are outflow facilities, R_0 is the resistance when IOP equals EVP, K_{ob} is the outflow obstruction coefficient. The equation for C_{uv} is a Michaelis-Menten type relation, where k_2 is the Michaelis constant for the flow rate (the pressure value for which the uveoscleral flow rate is half of k_1).

At the steady state value for IOP, the following relation must be true:

$$Q_{ah,uf} + Q_{ah,sec} = Q_{ah,tm} + Q_{ah,uv} \tag{3.14}$$

which can be solved considering IOP as the only unknown value. A global stochastic sensitivity was applied to the model computing variance-based sensitivity indices (also called Sobol indices, they give us an indication of the impact of a parameter's variation on IOP) using IOP probability distribution for four types of virtual subjects: ocular normotensive (ONT), ocular hypertensive (OHT), and both ONT and OHT that underwent IOP reduction medications (ONTm and OHTm). The results are shown in Figure 3.3.

OHT condition was simulated by using standard value C_0 multiplied by 0.3, decreasing trabecular meshwork outflow facility as suggested by clinical observations, while for medicated virtual subjects ionic secretion was decreased by 25%. In all cases, cBP and $\Delta\pi_s$ were the factors with higher Sobol indices, that is, higher effect on IOP with their variation. The effects of IOP lowering medications depended on the initial IOP of the subject. They also seemed to be more pronounced when AH production is affected rather than drainage.

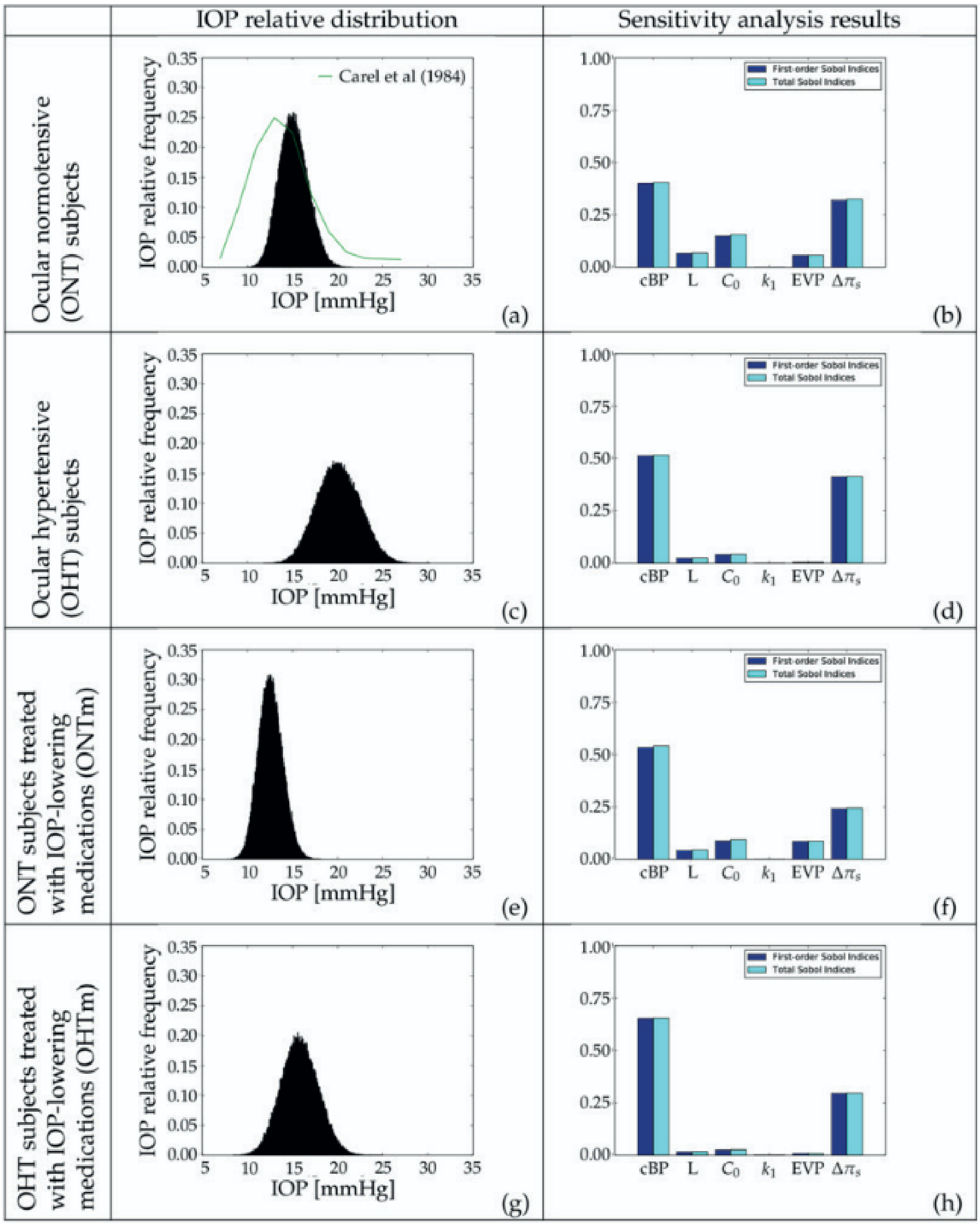

Figure 3.3: *Probability density functions for IOP and Sobol indices for cBP, L, C_0, k_1, EVP and $\Delta\pi_s$. Taken from [14]*

Chapter 4

Ocular hemodynamic models simulating microgravity

Microgravity is often simulated through varying degrees of head-down tilt (HDT), in which individuals are tilted head below feet at angles typically ranging from -6 to -30 degrees, mimicking the cephalad fluid shift experienced by astronauts in spaceflight. An example of HDT experimental setup can be seen in Figure 4.2.

Empirical data obtained through HDT experiments is then implemented in the equations of mathematical models, and microgravity can be simulated by explicitating either the gravitational vector and then changing its value or, in most cases, the angle of tilt θ and setting it to negative values reflecting HDT experiments.

In the next paragraphs, various models that simulate microgravity in the eye will be reviewed, studying the relationships between parameters like IOP, ICP, OPP and blood flow. Models range in complexity, from focusing only on the eye to implementing cerebral and cardiovascular systems.

4.1 Studying IOP in microgravity through a five-compartment model

Nelson et al. [16] proposed a model that is designed to predict the impact of increased ICP and ocular blood pressure on IOP. It considers the eye as an ensemble of compartments that interact with each adjacent other through fluid exchange or pressure differences, causing variations in compartmental volumes and pressures over time.

As can be seen in Figure 4.1, the eye globe is divided into five distinct compartments: the retrobulbar subarachnoid space (rSAS), that does not

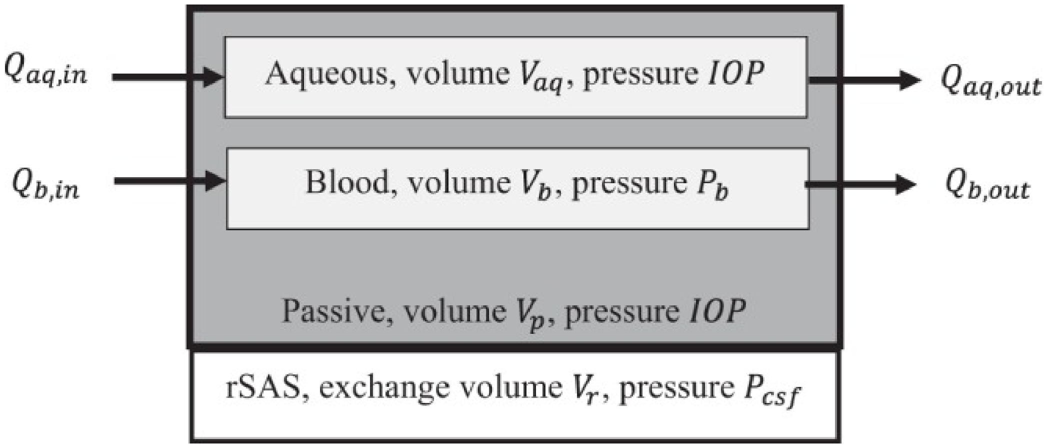

Figure 4.1: *Schematic of the lumped-parameter eye model. Taken from [16]*

exchange fluids with other compartments but can influence them through deformation driven by pressure differences and compliance; the passive compartment, which incorporates intraocular components that do not change in volume such as vitreous humor; the aqueous humor compartment; the blood compartment, divided in arterial and venous.

The anatomic reservoirs of blood in the eye are the choroid and the retina, and their contributions have been lumped together to form a generalized ocular blood volume. We take the arterial pressure as a function of the mean arterial pressure (MAP) of the cardiovascular system.

The influx of aqueous humor is considered constant, while the outflow depends on the outflow through the uvea and the one through the trabecular meshwork, which is a function of the trabecular meshwork's compliance and the difference between IOP and episcleral venous pressure (EVP).

The governing equations are six differential equations which are solved using a time-marching scheme:

$$\frac{dIOP}{dt} = \frac{1}{C_{g,\text{in vivo}}} F_g - \frac{1}{C_{g,\text{in vivo}}} C_{tm} IOP \tag{4.1}$$

$$F_g = C_{rg} \frac{dP_{csf}}{dt} + C_{ag} \frac{dP_a}{dt} + C_{vg} \frac{dP_v}{dt} + Q_{aq,in} + C_{tm} EVP - Q_{uv} \tag{4.2}$$

$$\frac{dV_{aq}}{dt} = Q_{aq,in} - C_{tm}(EVP - IOP) - Q_{uv} \tag{4.3}$$

$$\frac{dV_r}{dt} = C_{rg} \frac{d}{dt}(P_{csf} - IOP) \tag{4.4}$$

$$\frac{dV_b}{dt} = C_{ag} \frac{d}{dt}(P_a - IOP) + C_{vg} \frac{d}{dt}(P_v - IOP) \tag{4.5}$$

$$\frac{dV_g}{dt} = \frac{dV_b}{dt} + \frac{dV_{aq}}{dt} \tag{4.6}$$

Where Q_{aq} represents the flow of aqueous humor, and parameters called C are the different compliances. Most parameters were derived from literature, while others (such as blood-globe compliance) were calculated from other studies.

Ocular blood pressures have a major influence on the response of the model especially as gravity is changed. Cerebrospinal Fluid (CSF) pressure (CSFp) was considered constant since it only influences conditions in the eye through the rSAS-globe compliance (C_{rg}), which has an extremely small value. As conflicting data for MAP was found, two simulations were run: one with constant MAP and another one with time-varying MAP. The model does a surprisingly good job in its predictions, with good agreement with experimental data. Poorer agreement may be due to long-term regulatory processes not implemented in the model.

CSFp variations were found to be relatively unimportant when blood dynamics are in play, but they're expected to have large influence on biomechanical strain on posterior eye tissues. This model doesn't include autoregulation and suffered the scarce availability of comprehensive experimental.

4.1.1 Implementing HDT experimental measures

The previous eye model was further advanced by Petersen et al. [17], taking into account ocular perfusion pressure (OPP), calculated as the difference from the MAP measured at the entrance of the eye (MAP_{eye}) and IOP.

Reduced OPP due to low MAP_{eye} or high IOP is a well-known risk factor for glaucoma. Since the eye is a smaller hydrostatic system than systemic circulation, changes in gravitational vector have less an effect on IOP rather than on MAP_{eye}. The authors studied the effect of posture on pressures in

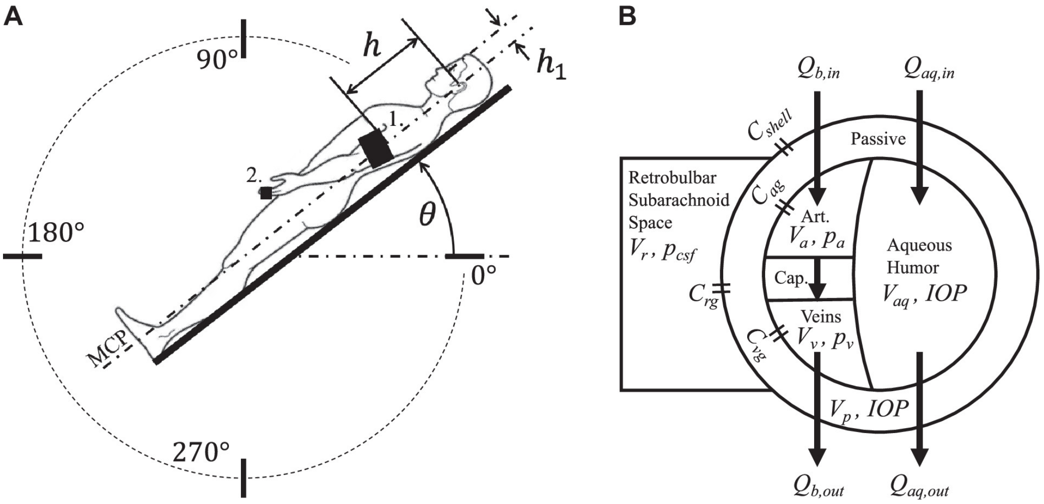

Figure 4.2: *A) Shows the setup used for HDT experiments; B) Shows a schematic of the lumped-parameter model used. Taken from [17]*

the eyes and found that not only postural changes, but also position (prone vs supine) affects ocular hemodynamics by inducing a hydrostatic column from the base of the rostral globe to the mid-coronal plane (see Figure 4.2).

It is hypothesized that high OPP due to mismatch between the autoregulation of MAP_{eye} and IOP leads to swelling of the hyperemic choroid, and thus it would be an important factor in the etiology of SANS. Changes on gravitational vector's effects on IOP and MAP_{eye} are investigated using a modified version of the model proposed in [16]. The difference with the original version is the method used to calculate EVP, which here is calculated using an empirical approach to account for otherwise unaccounted regulatory changes. EVP here is also a function of the distance between the rostral globe and the mid-coronal plane, which is found to hold a noticeable significance as it's the main factor that differentiates prone vs supine position. No changes were made to the parameters given in Nelson et al. [16] except that MAP_{eye} was adjusted to represent the population of this study.

The authors performed measurements on a group of 13 males, during head-down tilt (HDT) and head-up tilt (HUT), then ran a statistical analysis on the results, by comparison to which the model was validated. Taking by reference the supine horizontal position, it was found that that IOP suffers a statistically significant decrease of around $-3.3 \pm 0.6mmHg$ when the subject is tilted upright, but no other significant changes were noted in a head upwards position, while a significant increase in IOP was noted in head downwards positions, especially in a fully inverted position (increase of $20.71.7mmHg$). MAP_{eye} was found to follow a similar trend. At low HDT angles, it was found that OPP significantly differs between prone and supine positions, but at higher HDT angles this difference becomes statistically insignificant. Thus, IOP and MAP_{eye} were determined to be gravitationally dependent variables.

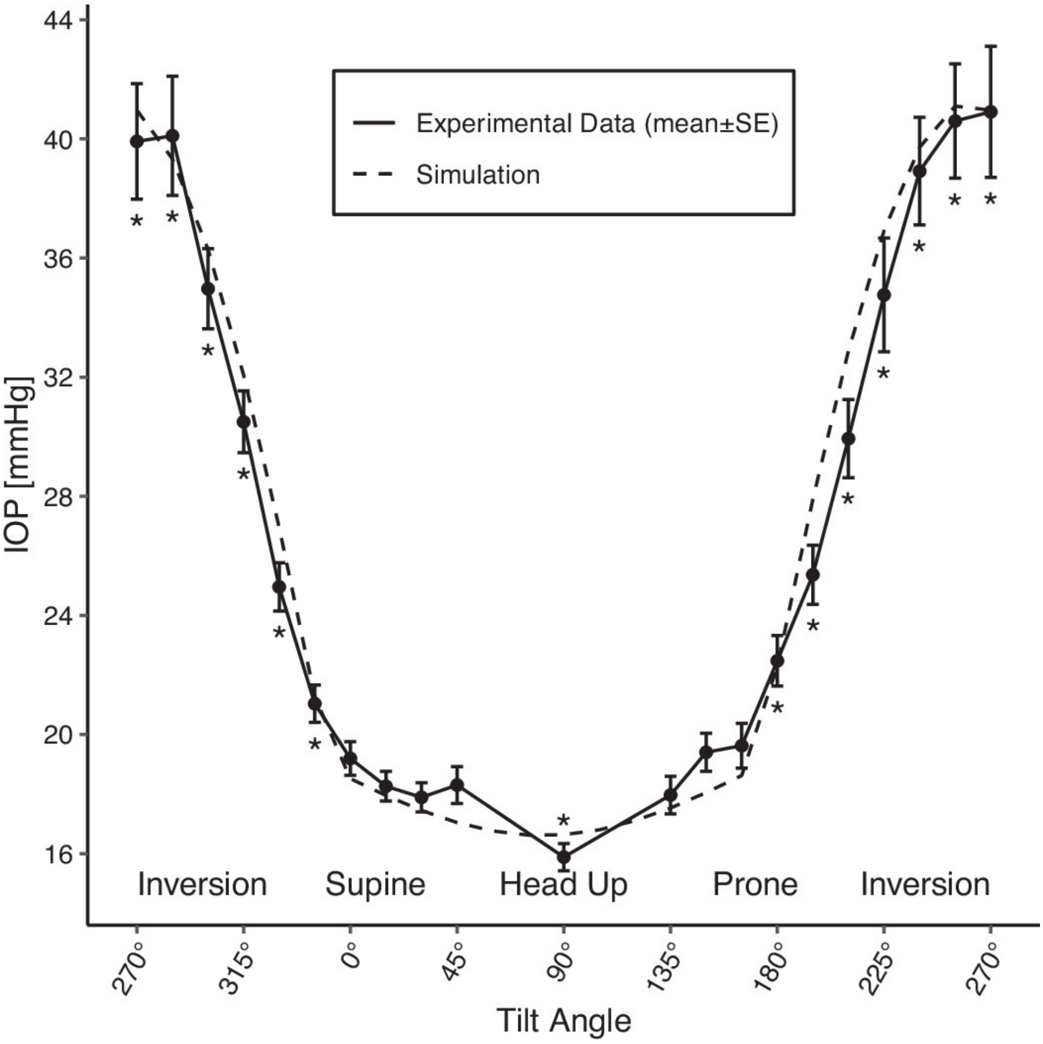

Figure 4.3: *IOP as a function of tilt angle across 13 male subjects. Taken from [17]*

OPP was confirmed to decrease when in upright position and increase when in fully tilted position, with respect to supine horizontal position. IOP measurements (see Figure 4.3) were similar to those predicted by the model, with differences likely due to the timescale of the experiment, and thus due to regulatory processes not accounted for in the model.

The confirmed increase of IOP from supine to prone position supports the conclusion that hydrostatic forces play an important role in studying the possible causes of SANS, as high OPP can be correlated to early signs of SANS. The study suggests that chronically elevated OPP resulting from changes in passive hydrostatic forces may contribute to optic disc edema in SANS.

The significant dependency on the gravitational vector of IOP and OPP implies the pressure and flow regulation of ocular tissues are affected by gravitational variations. Continuous exposure to microgravity conditions may result in a mild but constant state of augmented perfusion to the ocular tissue. Though limited by the data on whether the regulation mechanisms can be explained with passive hydrostatics or with an active regulation system, this study suggests much of short-term gravitational effects on ocular pressure and perfusion can be explained by passive hydrostatics. Another limitation was the population of the study: only male subjects of young age, below the average age of flight-status astronauts. Unfortunately, the sample size of female astronauts is still too small to determine if sex is a risk factor

4.2 Coupling eye and brain systems

Salerni et al. [10] proposed a model that takes into account changes in cerebral flow. It displays a more complex description of fluid circulation in the eyes and their connections to the brain, through an electric equivalent that can be seen in Figure 4.4.

The brain and eyes share vessels for blood supply and drainage. The blood flow in the eyes is divided within three ocular vascular beds: the retina; the choroid; the ciliary body. CSF influences the tissue pressure in the optic nerve head and in lamina cribrosa (LC) biomechanics. The model investigates the relationship between IOP, ICP and CSFp, as well as the flow of fluids between eyes and brain.

To predict fluid redistribution in upper body vasculature and variations in IOP and ICP following exposure to microgravity, the lumped-parameter model presents three main components: both eyes, the brain and a simplified model of the upper body. The main difference in the eye model from Nelson et al. [16] is the characterization of three different blood vessels: the retina, itself subdivided in the central retinal artery and the central retinal vein, the choroid and the ciliary body.

The brain sector considers blood, CSF and interstitial fluid. The model neglects time variations on both short time scale of heart beats and long time scale of remodelling processes, as well as autoregulation mechanisms of small vessels. Both filtration of interstitial fluid from capillaries to interstitial space and filtration of aqueous humor from ciliary body capillaries to posterior

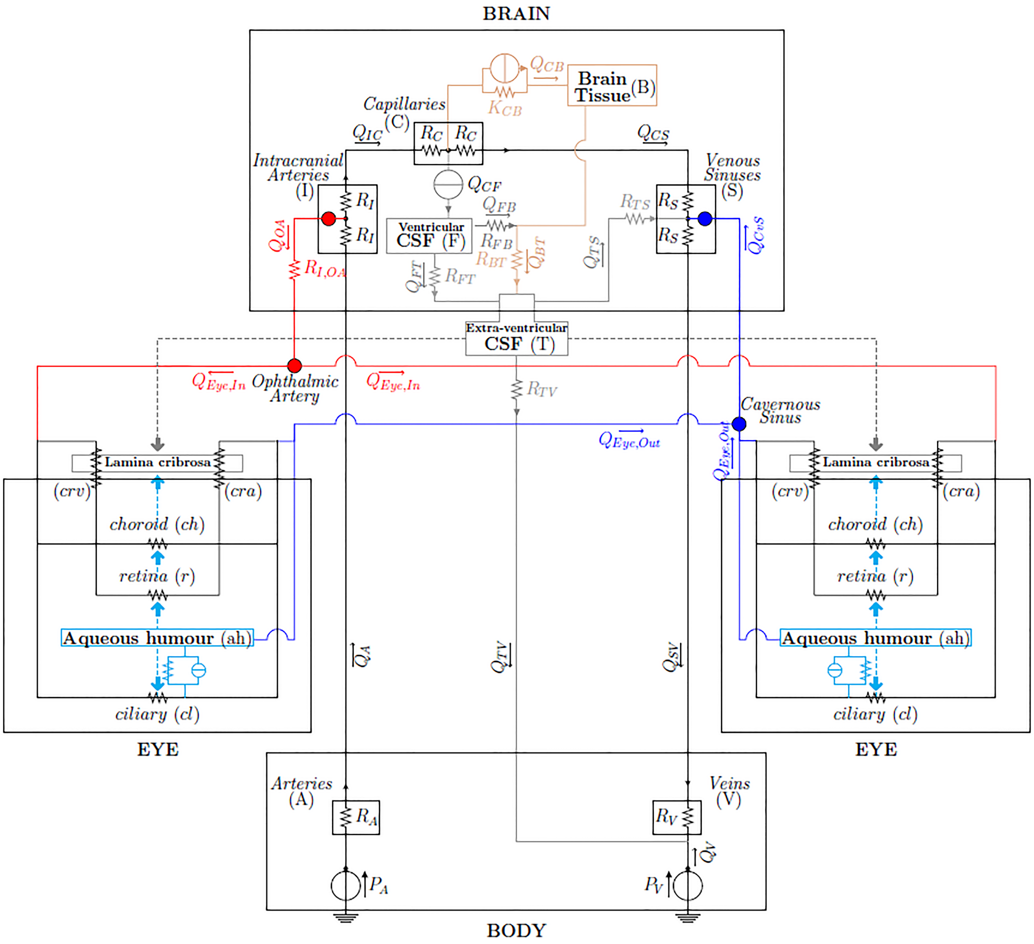

Figure 4.4: *Lumped-parameter model showing the nodes connecting eye and brain systems. Taken from [10].*

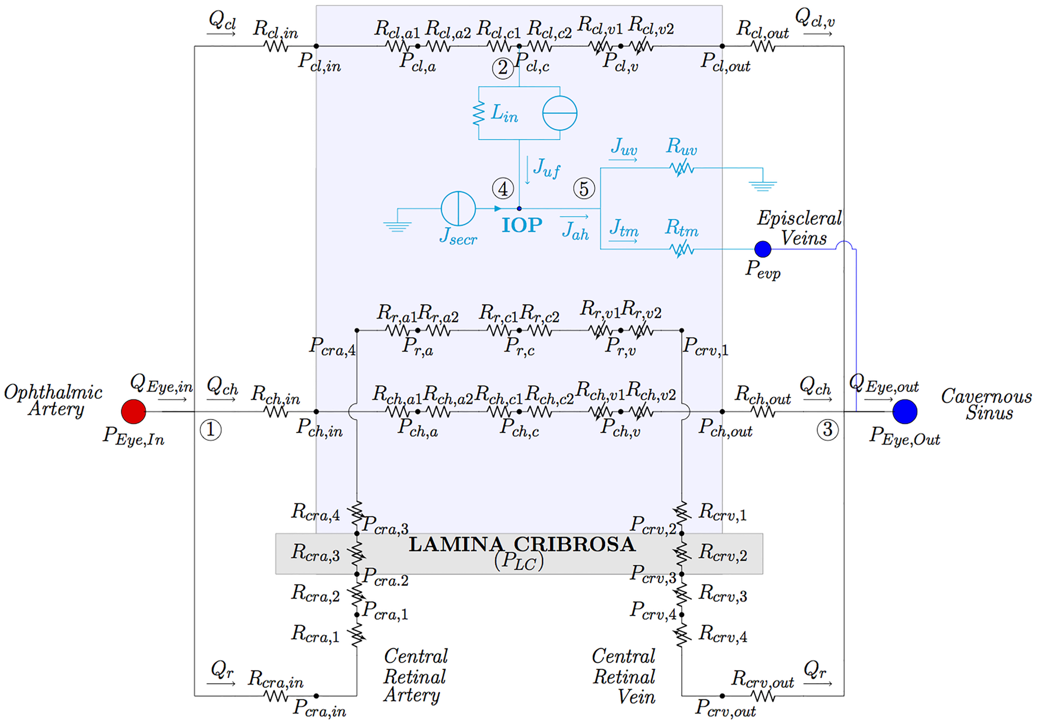

Figure 4.5: *Eye circuit in detail. Taken from [10]*

and anterior chambers of the eye are accounted for using the Starling-Landis equation. CSF production is kept constant, and cerebral blood flow is allowed to vary. The Lakin and Stevens model [18] was adopted for cerebral fluid-dynamics, which doesn't account for collapsibility of internal jugular veins and the presence of lymphatic and glymphatic systems. The eye model proposed presents two interconnecting circuits, specifically that of aqueous humor and that of blood. For arterioles and capillaries constant resistances are used, calculated using Poiseuille's law, while for passive changes in vascular diameter (and possibly in the shape of the cross-sectional area) due to the action of transmural pressure differences variable resistances are considered.

A detail of the eye lumped-parameter model can be seen in Figure 4.5, where the grey-shaded area represents the LC. We can observe the influence of the aqueous humor circuit on the blood circuit via IOP, while the blood circuit influences the aqueous humor circuit via pressure in the ciliary body. The coupling of eyes and brain happens through the ophthalmic artery, the cavernous sinus and episcleral veins connection to the venous sinus, and the action on the lamina cribrosa through IOP from the ocular side and through CSFp from the subarachnoid space.

Microgravity was simulated, and its consequences seemed to prevent the normal lowering of ICP when standing upright. The model was calibrated through a large data set, and the reference for the model is the supine position. The model predicted, in agreement with experimental data, an increase in IOP as a consequence of increased blood pressure, as well as a decrease in ICP as a consequence of decreased blood pressure. Blood oncotic pressure changes were used as a reference for gravitational vector variation, as it probably decreases in microgravity. We can observe an increase in both ICP and IOP as the oncotic pressure drops. If IOP grows too much, vessels start to collapse.

Despite its many limitations, this model proved capable of simulating the relationships between IOP, CSFp and blood pressure reported in major studies. It can be used to investigate changes in flow and pressure distributions associated with long-term exposure to microgravity. In this regard, it can be used as complementary to the model by Nelson et al. [16].

4.3 Integrating cerebral and ocular hemodynamics with cardiovascular system responses to head-down tilt

To better understand the relationship between ICP and IOP, Fois et al. [19] proposed a model that integrated their previous human cardiovascular (CVS) framework with lumped-parameter models of ocular compartments and cerebrovascular circulation. The model can be seen in Figure 4.6. Simulations were then ran for varying degrees of inclination: from 80 degrees HUT to 6 degrees HDT.

Increasing pressure from 80 HUT to 6 HDT degrees case was higher in cerebral arterial pressure than in eye arterial pressure. This can be explained by the eye's position with respect to the body's mid-coronal plane. Mean eye venous pressure also was found to increase by +260% . Overall increases in pressure can be explained by decreased arterial and venous cerebral compliance.

Blood flow rates, conversely, show a much more homogenous response to HDT: while at first there is a reported increase, it is rapidly settled down to almost pre-tilt levels. This is due to autoregulation mechanisms of the CVS and cerebrovascular system, and shows the importance of such processes in regulating hemodynamics in microgravity conditions. This is true for mean flow rates, while pulse flow rates show an overall increase.

Both IOP (15.8 mmHg to 19.9 mmHg) and ICP (-0.1 mmHg to 10.9 mmHg) increase in HDT conditions, but the latter is reported to increase more, with consequently decreasing translaminar pressure, which is deemed

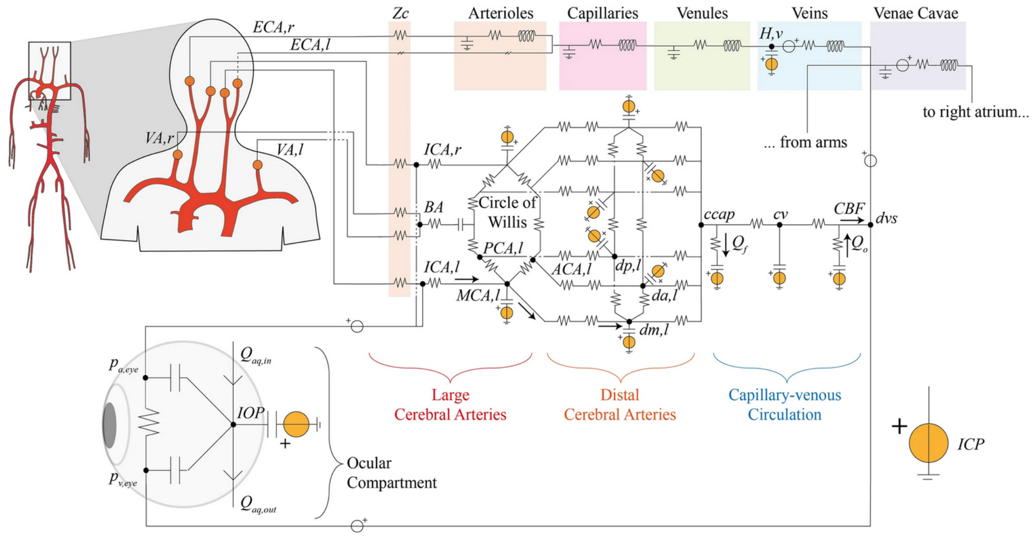

Figure 4.6: *1D arterial network (on the left) connected with the 0D lumped-parameter head, cerebral and ocular compartments.* Z_c *represents lumped characteristic impedances. Taken from [19]*

as a possible contributor to SANS development. At the same time, OPP measures an increase from 49.6 mmHg to 65.1 mmHg, as the increase in eye arterial pressure overcomes the one in IOP. This could lead to risks for optic disk edema in microgravity conditions.

Due to headward fluid shifts, both cerebral and extra-cerebral venous volumes increase during HDT, while ocular globe volume measures almost no volume change. Thus, while IOP increases, eye volume remains almost unchanged, but cerebral and extra-cerebral blood volume increases, underlining how the retrobulbar space can exert higher compression forces on the ocular globe, possibly inducing structural changes over prolonged time.

The model predicts a decrease in translaminar pressure in HDT conditions, which, depending on the subject's initial ICP, can even become negative, impairing normal equilibrium between the eye globe and the retrobulbar space, as well as OPP.

As Fois et al. note [19], CO_2 levels, given the molecule's cerebrovascular dilation properties, should be implemented in future models. Also, differences exist between HDT and actual microgravity, for example CVP that increases in HDT but actually decreases in microgravity conditions.

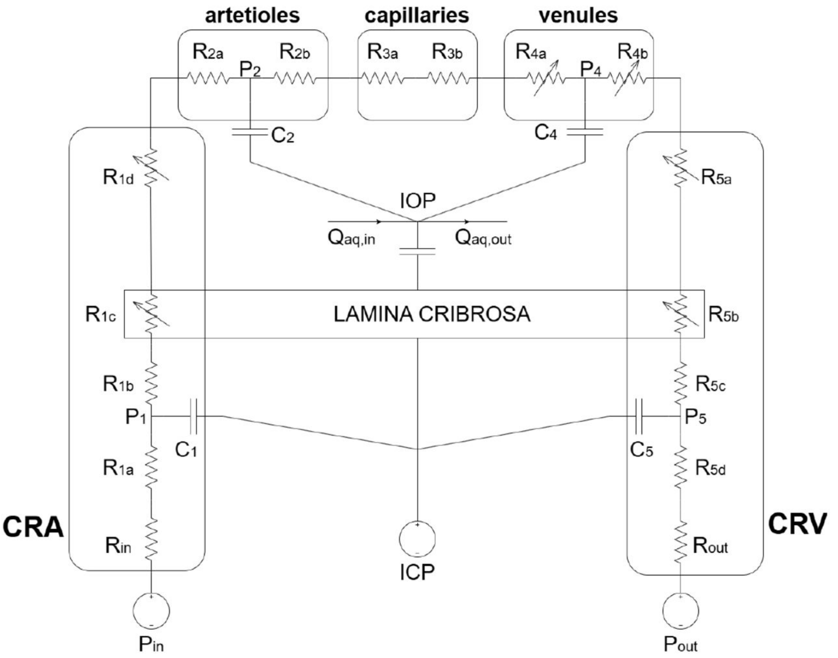

Figure 4.7: *Lumped-parameter model of retinal hemodynamics taken from [20]*

4.4 Retinal hemodynamics in microgravity conditions

A model for retinal hemodynamics in microgravity conditions was proposed by Nigro et al. [20] further advancing precedent models that lacked either lacked microgravity conditions [9] or consideration of interaction with retinal vasculature [10, 16, 17, 19].

The lumped-parameter model proposed by Nigro et al. can be viewed in Figure 4.7, where we can see the integration of the model proposed by [9] with IOP and AH dynamics. Retrolaminar tissue pressure is assumed to be equal to ICP. IOP is considered a dynamic state variable, with arterial blood pressure considered as the input variable. For estimation of P_{in}, this model adopts the patient-specific one proposed by Guidoboni et al. [9], while for estimation of P_{out} the condition proposed by Petersen et al. [17] was adopted. To account for HDT, hydrostatic pressure was calculated and added to P_{in} to get $P_{in,\theta}$ specific to the angle of HDT. For EVP variation, the empirical relationship descripted in [16] was adopted:

$$EVP = 9.0\ mmHg - \alpha sin(\theta) \tag{4.7}$$

where α depends on the inclination regime (22.1 mmHg for $\theta \leq 0$ and 2.23

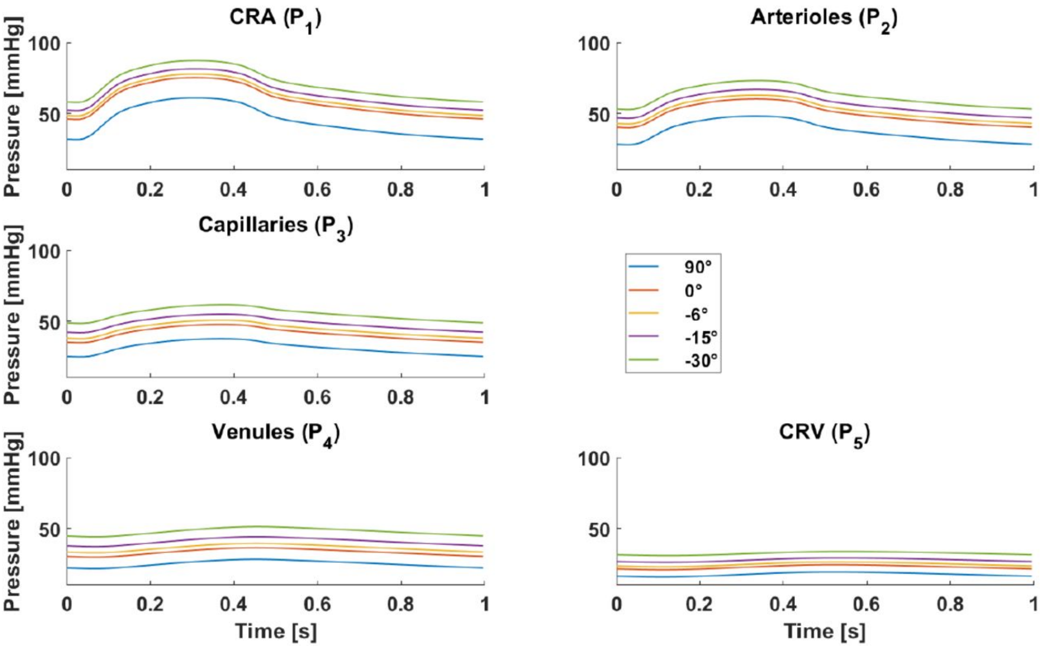

Figure 4.8: *Pressure curves predicted for the five compartments of retinal vasculature at different tilt angles. Taken from [20]*

mmHg for $\theta > 0$). Velocity in the CRA was modeled after the following relationship:

$$v_{\text{CRA}}(t) = \frac{8}{\pi D_{\text{CRA}}^2} \cdot \frac{P_{\text{in}}(t) - P_1(t)}{R_{\text{in}} + R_{1a}}, \tag{4.8}$$

Comparing IOP results with the experimental campaign values obtained by Petersen et al. [17], the model seems to simulate well primary features of IOPvsHDT relationship. MAP_{eye} was derived from experimental measurements in [9] and increased due to hydrostatic redistribution to account for different tilt angles. Pressure calculation results can be seen in Figure 4.8.

It can be noted that pressure increases gradually with decreasing tilt angle, while the waveform becomes more damped moving through arterioles to capillaries and venules to CRV. At $\theta = -30°$ pressures are significantly higher than at $\theta = 90°$, which may compromise retinal perfusion, leading to hypoperfusion, oxidative stress and inflammation.

Initial simulations of velocity didn't show good accordance with reference experimental literature, but a correction in the CRA diameter of -4%, as motivated by experiments on parabolic flights by Mader et al. [21] resulted in velocity predictions following the experimentally observed trend. This suggests that vascular modifications due to microgravity are essential to accurately describe ocular hemodynamics in this environment. Reults from retinal blood flow calculations showed it remained relatively stable, reinforcing the hypothesis that retinal circulation is effectively autoregulated across a range of perfusion pressures and inclinations.

Flow rate, PSV and EDV decreased with HDT, while vascular RI increased.

As noted in the study, important factors that can interfere with ocular hemodynamics in space are still not implemented in mathematical models, like radiation-induced ocular changes.

Chapter 5

Conclusions

Ocular responses to microgravity are complex and directly influenced by responses in the whole body as well as external factors.

Based on results from the reviewed models, some assumptions can be made, but it must be taken into account that these are all short-time simulations, and responses to longer periods of time in microgravity need to be investigated to make more valid hypotheses.

Reviewed models have consistently shown that IOP is subject to an acute increase when going from normal conditions to simulated microgravity, possibly due to altered venous drainage and fluid shift towards the upper body. This could mean that excessive stress may be put on tissues. It is also noted that elevated IOP is a known risk factor for glaucoma.

Along with IOP, ICP also seems to increase, though to varying degrees depending on the model assumptions and individual subject. The resulting variation in translaminar pressure may disrupt the biomechanical equilibrium through the LC, potentially contributing to optic disc edema.

It is important to note an increase in OPP that could be significant for developing SANS: while retinal flow seems to be well auto-regulated (though retinal perfusion may be compromised [20]), chronic elevation in OPP would likely lead to optic disc swelling and structural stress on the posterior eye.

The integration of cerebral and cardiovascular systems highlights the importance of regulatory mechanisms across the body. Though significant progression has been made in simulating short-term response to microgravity, there are still various factors unaccounted for. The most troubling problem in understanding SANS pathophysiology is the lack of integrated long-term response mechanisms, which may provide useful new information in the relationship between hemodynamic parameters, as can be assumed by experiment results reported in NASA's evidence report [1].

Spaceflight exposure to a higher carbon dioxide percentage than in Earth's atmosphere may also play a role in the vascular regulatory system, as well as radiation exposure.

In summary, though still needing more experimental data and more integrated models, research suggests that acute variations in IOP and ICP, and thus OPP resulting from the lack of a gravitational vector are likely to be one of the causes of the onset of SANS.

List of Figures

Bibliography

[1] Stenger M. B. and Tarver H. W. J. Human research program - human health countermeasures element. Technical report, National Aeronautics and Space Administration Lyndon B. Johnson Space Center Houston, Texas, 2017.

[2] Jie Zhu, Ellean Zhang, and Katia Rio-Tsonis. *Eye Anatomy.* 11 2012.

[3] Adamantios Michalinos, Sofia Zogana, Evangelos Kotsiomitis, Antonios Mazarakis, and Theodore Troupis. Anatomy of the ophthalmic artery: A review concerning its modern surgical and clinical applications. *Wiley Online Library*, 2015.

[4] Hayreh SS and Dass R. The ophthalmic artery: I. origin and intra—cranial and intra—canalicular course,. *The British Journal of Ophthalmology*, 46(2):65–98, 1962.

[5] Akdemir Aktaş H, Mine Ergun K, Tatar İ, Arat A, and Mutlu Hayran K. Investigation into the ophthalmic artery and its branches by superselective angiography. *Interv Neuroradiol*, 2022.

[6] Bingqiang Xu and Huitong Liu. The three-dimensional computed tomography anatomic features of internal carotid artery–ophthalmic artery. *J Craniofac Surg*, 30:1609–1611, 2019.

[7] Ambarki K, Hallberg P, Johannesson G, et al. Blood flow of ophthalmic artery in healthy individuals determined by phase-contrast magnetic resonance imaging. *Invest in Opthalmol Vis Sci.*, 2013.

[8] Shi Yubing, Lawford Patricia, and Hose Rodney. Review of zero-d and 1-d models of blood flow in the cardiovascular system. *BioMedical Engineering OnLine*, 2011.

[9] Guidoboni G, Harris A, Cassani S, et al. Intraocular pressure, blood pressure, and retinal blood flow autoregulation: A mathematical model

to clarify their relationship and clinical relevance. *Invest Ophthalmol Vis Sci.*, 55:4105–4118, 2014.

[10] Fabrizia Salerni, Rodolfo Repetto, Alon Harris, Peter Pinsky, Christophe Prud'homme, Marcela Szopos, and Giovanna Guidoboni. Biofluid modeling of the coupled eye-brain system and insights into simulated microgravity conditions. *PLOS ONE*, 14(8):1–29, 08 2019.

[11] Takahashi T, Nagaoka T, Yanagida H, et al. A mathematical model for the distribution of hemodynamic parameters in the human retinal microvascular network. *J Biorheol.*, 23:77–86, 2009.

[12] Lakin WD, Stevens SA, Tranmer BI, and Penar PL. A whole-body mathematical model for intracranial pressure dynamics. *J Math Biol.*, 46:347–383, 2003.

[13] He Z, Nguyen CT, Armitage JA, Vingrys AJ, and Bui BV. Blood pressure modifies retinal susceptibility to intraocular pressure elevation. *PLoS One*, 7:e31104, 2012.

[14] Marcela Szopos, Simone Cassani, Giovanna Guidoboni, Christophe Prud'Homme, Riccardo Sacco, et al. Mathematical modeling of aqueous humor flow and intraocular pressure under uncertainty: towards individualized glaucoma management. *Journal for Modeling in Ophthalmology*, 2:29–39, 2016.

[15] Brubaker R. The effect of intraocular pressure on conventional outflow resistance in the enucleated human eye. *Invest Ophthalmol*, 1975.

[16] Nelson ES, Mulugeta L, Feola A, Raykin J, Myers JG, Samuels BC, and Ethier CR. The impact of ocular hemodynamics and intracranial pressure on intraocular pressure during acute gravitational changes. *J Appl Physiol*, 2017.

[17] Petersen LG, Whittle RS, Lee JH, Sieker J, Finke C Carlson J, Shelton CM, Petersen JCG, and Diaz-Artiles A. Gravitational effects on intraocular pressure and ocular perfusion pressure. *J Appl Physiol*, 2022.

[18] William D. Lakin and Scott A. Stevens. *Modelling the Response of Intracranial Pressure to Microgravity Environments*, pages 211–227. Birkhäuser Basel, Basel, 2008.

[19] Fois Matteo, Diaz-Artiles Ana, Zaman Syeda Yazmin, Ridolfi Luca, and Scarsoglio Stefania. Linking cerebral hemodynamics and ocular

microgravity-induced alterations through an in silico-in vivo head-down tilt framework. *npj Microgravity*, 2024.

[20] Michele Nigro, Andrea Montanino, and Eduardo Soudah. A computational model for retinal hemodynamics under gravitational and postural variations. *bioRxiv*, 2025.

[21] Mader TH, Gibson CR, Caputo M, Hunter N, Taylor G, Charles J, et al. Intraocular pressure and retinal vascular changes during transient exposure to microgravity. *American Journal of Ophthalmology*, 1993.